

Effect of the Secondary Rutile Phase in Single-Step Synthesized Carbon-Coated Anatase TiO₂ Nanoparticles as Lithium-Ion Anode Material

Adele Birrozzi, Raffaella Belchi, Johann Bouclé, Dorin Geiger, Ute Kaiser, Stefano Passerini, Nathalie Herlin-Boime,* and Dominic Bresser*

TiO₂ has been investigated as an alternative anode material candidate for lithium-ion batteries for several years now due to its advantageous safety and rate capability in combination with its nontoxicity and abundance. Herein, the synthesis via laser pyrolysis is reported, which allows the single-step, industrial-scale realization of carbon-coated TiO₂ nanoparticles. The modification of the synthesis parameters enables the variation of the rutile-to-anatase phase ratio. Following comprehensive physicochemical and electrochemical characterization, both the higher and lower rutile-to-anatase ratios show very stable cycling in lithium battery half cells, whereas the extended presence of the rutile phase limits the achievable specific capacity and lowers the apparent lithium-ion diffusion coefficient, which leads to relatively lower capacities at elevated current densities.

while LTO is already used in commercial LIBs,^[4,18] Li-free TiO₂ is still at the research level—not least due to the greater variety in available polymorphs, i.e., anatase, rutile, and TiO₂(B), to name just the most investigated ones for their potential use as active materials in LIBs.^[7,11,16,19,20] Out of these three, anatase and rutile are naturally occurring phases and, thus, of particular interest.^[11,16] Nevertheless, the rutile phase shows suitable specific capacity and electrochemical performance only when using very fine nanoparticulate materials and the de-/lithiation potential varied by more than 1 V,^[21,22] rendering it less applicable when targeting a (rather) constant cell voltage. In contrast, anatase TiO₂ is


characterized by a constant lithiation potential at about 1.8 V corresponding to the anatase-to-titanate phase transition.^[23–25] In the case of sufficiently small nanoparticles, an additional phase transition may occur beyond the lithiation up to Li_{0.55}TiO₂, i.e., the further lithiation to anatase Li₁TiO₂.^[26–29] These characteristics render anatase TiO₂ generally favorable for practical applications. Nonetheless, the rather similar thermodynamic stability of the two polymorphs, especially at the nanoscale,^[30–32] results in a challenging large-scale synthesis of phase-pure anatase TiO₂—even more so, when considering the various approaches to further optimize the electrochemical performance, including the introduction of dopants or defects as well as the realization of smartly designed and well-elaborated nanostructures and nanocomposites.^[20,33–38] In fact, even the well-established

1. Introduction

Latest since the commercialization of lithium-ion batteries (LIBs) in 1991, a plethora of potential active materials have been investigated, targeting reduced cost as well as further improved energy and power densities, cycle life, safety, and sustainability.^[1–4] Of particular interest have been environmental benign and abundant titanium oxides such as Li₄Ti₅O₁₂ (LTO) and TiO₂, as they are characterized by a very little-to-essentially negligible volume variation upon de-/lithiation and offer very good rate capabilities as well as suitably high capacities at elevated de-/lithiation potentials of about 1.6 V (LTO) and 1.9 V (exemplarily for anatase TiO₂) versus Li⁺/Li, thus offering an intrinsic safety feature with regard to the risk of potential lithium plating.^[4–17] However,

A. Birrozzi, Prof. S. Passerini, Dr. D. Bresser
Helmholtz Institute Ulm (HIU)
Helmholtzstrasse 11, Ulm 89081, Germany
E-mail: dominic.bresser@kit.edu

A. Birrozzi, Prof. S. Passerini, Dr. D. Bresser
Karlsruhe Institute of Technology (KIT)
P.O. Box 3640, Karlsruhe 76021, Germany

 The ORCID identification number(s) for the author(s) of this article can be found under <https://doi.org/10.1002/ente.202001067>.

© 2021 The Authors. Energy Technology published by Wiley-VCH GmbH. This is an open access article under the terms of the Creative Commons Attribution License, which permits use, distribution and reproduction in any medium, provided the original work is properly cited.

DOI: 10.1002/ente.202001067

Dr. R. Belchi, Dr. N. Herlin-Boime
CEA Saclay
IRAMIS, NIMBE, UMR 3685
Univ. Paris Saclay
Gif Sur Yvette 91191, France
E-mail: nathalie.herlin@cea.fr

Dr. R. Belchi, Dr. J. Bouclé
CNRS, UMR 7252, XLIM
Univ. Limoges
Limoges 87000, France

Dr. D. Geiger, Prof. U. Kaiser
Central Facility for Electron Microscopy
Ulm University
Ulm 89081, Germany

application of carbonaceous coatings that allow for healing surface defects and substantial performance improvements requires additional processing and post-treatment steps,^[33,39–43] rendering such strategies very promising at the laboratory scale but of limited use for industrial-scale applications.

Herein, we report the single-step synthesis of carbon-coated TiO₂ nanoparticles via laser pyrolysis as a scalable synthetic route. In addition to the facile scalability of this process, already realized at the industrial scale for, e.g., Si^[44] (but not yet for carbon-coated TiO₂ so far), this method allows for continuous material production. Moreover, there is no need for any further processing or thermal treatment of the material, which provides significant cost advantages.^[45,46] By optimizing the synthesis parameters, we have been able to reduce the ratio of the rutile phase to less than 10%, which results in substantial improvement in terms of achievable specific capacity and rate capability due to the faster (apparent) lithium-ion diffusion.

2. Results and Discussion

2.1. Physicochemical Characterization

The general setup of laser pyrolysis is schematically shown in **Figure 1**. The synthesis of the two TiO₂ samples differentiated only in one experimental parameter: the mass flow rate of the sensitizer C₂H₄, being either 355 sccm in the case of A50R50 and 300 sccm in the case of A90R10. As an immediately apparent consequence of the modified mass flow rate, we noticed a different color of the flame, changing from yellow–orange (355 sccm) to a more transparent flame (300 sccm). This phenomenon indicates that a higher reaction temperature was reached in the former case, i.e., when the mass flow rate was higher. This higher reaction temperature led to a higher production rate of 3.97 g h^{−1} compared with 1.13 g h^{−1} in the latter case. Accordingly, there is a strong impact of the C₂H₄ mass flow rate on reaction efficiency. To investigate any potential further difference between these two samples, we conducted X-ray diffraction (XRD) analysis on the powders. The direct comparison of the two diffractograms (**Figure 2a**) reveals that both samples are mainly composed of anatase TiO₂ (space group: *I4₁/amd*). Nevertheless, especially

for A50R50, there is substantial contribution of rutile TiO₂ (space group: *P4₂/mmm*), which is greatly decreased in the case of A90R10. A closer inspection of the XRD data using the GSAS software allowed to roughly quantify the anatase-to-rutile ratio to be about 50:50 in the case of A50R50. For A90R10, the ratio of anatase TiO₂ was more than 90% and, consequently, less than 10% for the rutile phase. In fact, this ratio is reflected also in the sample names (A for anatase and R for rutile). Generally, this finding is in good agreement with the earlier observation of the higher reaction temperature in the case of A50R50. The higher mass flow rate of the sensitizer enables a more efficient absorption of the laser, leading to higher temperatures (similarly to a previous study where the laser power was tuned^[47]). Consequently, more energy is transferred to the TTIP droplets, resulting in better dissociation in the reaction zone and, eventually, the tendency of a greater ratio of the rutile phase as the thermodynamically favored one.^[30,31] The crystallite size, however, is fairly similar for both samples with about 10–20 nm in both cases, as determined via the Scherrer equation (1).

$$L = \frac{K\lambda}{B_{2\theta} \cos \theta} \quad (1)$$

with $B_{2\theta}$ as the line broadening at half the maximum intensity (FWHM) at a particular 2θ value, λ as the X-ray wavelength, K as a dimensionless constant that is commonly set to 1 for (almost) spherical particles, and L as the crystallite size.

To check whether the nanoscale dimensions are reflecting only the crystallite size or also the particle size, the two samples were also studied via scanning electron microscopy (SEM) (**Figure 2b–g**). Both A50R50 (**Figure 2b–d**) and A90R10 (**Figure 2e–g**) are composed of essentially spherical (some slightly elongated) nanoparticles with a diameter of about 10–50 nm, which is in good agreement with the Scherrer analysis and, thus, indicates that the particles are essentially single crystalline. In addition, a few larger, microsized spherical particles were observed in both samples (not shown herein), which we attribute to TTIP droplets that did not intersect with the laser beam and reacted when exposed to air after the synthesis.^[46] Energy-dispersive X-ray spectroscopy (EDX) mapping reveals a homogenous distribution of oxygen, titanium, and carbon, for both A50R50 (**Figure 3a**) and A90R10 (**Figure 3b**), underlining the suitability of this synthesis method for the realization of evenly carbon-coated TiO₂ nanoparticles.

The findings of the SEM analysis were generally confirmed by the subsequent high-resolution transmission electron microscopy (HRTEM) investigation, showing particles of a comparable size and high crystallinity (**Figure 4**). In the case of A50R50, however, some of the particles appeared to show some “nanoscale porosity” or defects (**Figure 4a**), which cannot be (solely) explained by a potential beam damage, as it was observed right from the beginning of the analysis and did not increase noticeably during the experiment. We assume that these defects are the result of the higher flow rate of the sensitizer, leading to a higher reaction temperature and, thus, faster oxidation—an effect that generally favors the presence of defects. The consequently extended presence of the rutile phase presumably also contributes to this finding. In addition, a few-nm-thin amorphous layer

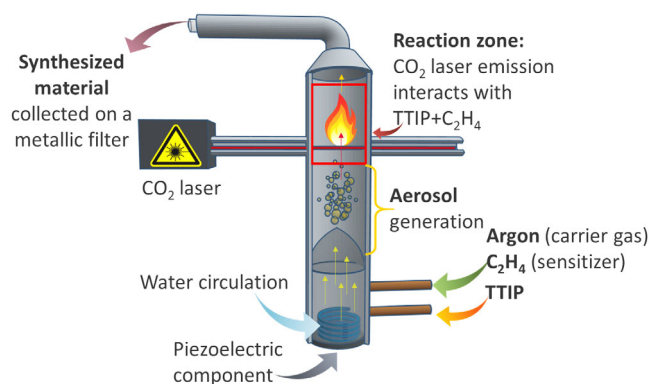


Figure 1. Schematic illustration of the laser pyrolysis setup used for the single-step synthesis of carbon-coated TiO₂ nanoparticles.

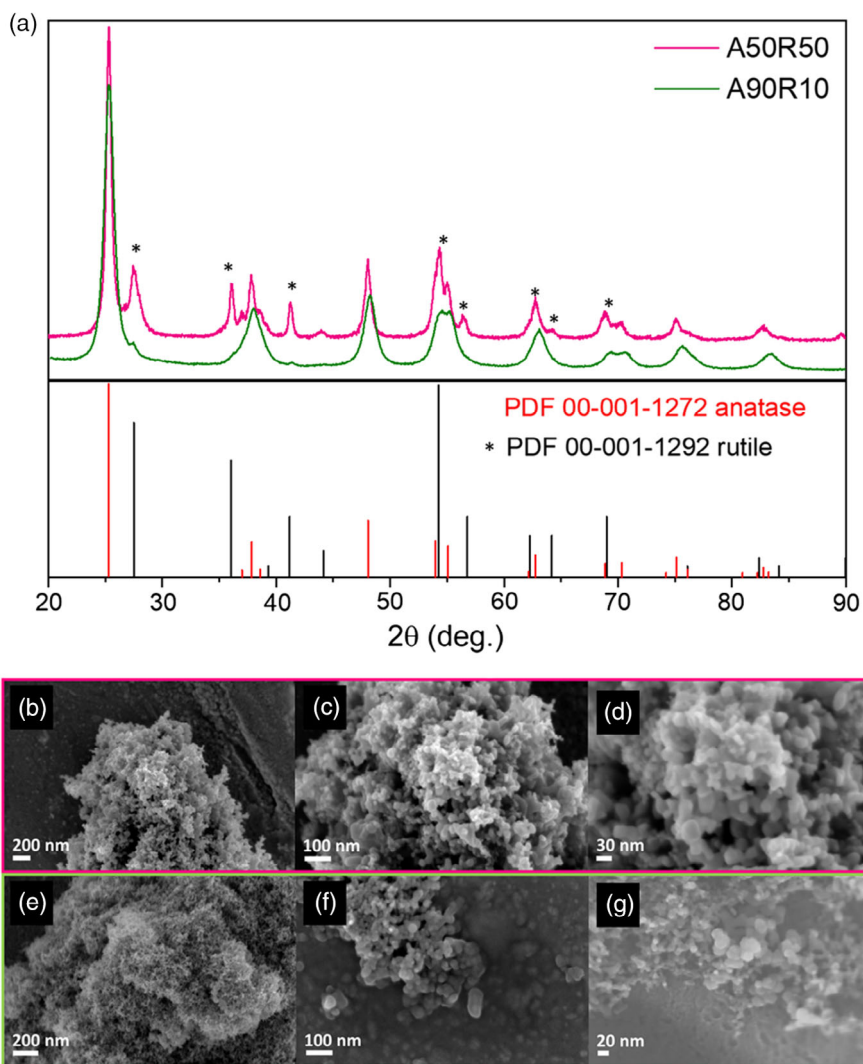


Figure 2. a) Comparison of the X-ray diffractograms of A50R50 (in pink) and A90R10 (in green); in the bottom, the PDF references for anatase (00-021-1272, in red) and rutile (00-0001-1292, in black) TiO_2 are provided; in addition, the reflections related to rutile TiO_2 are indicated by an asterisk in the diffractograms. b–g) SEM images of (b–d) A50R50 and (e–g) A90R10 at different magnifications.

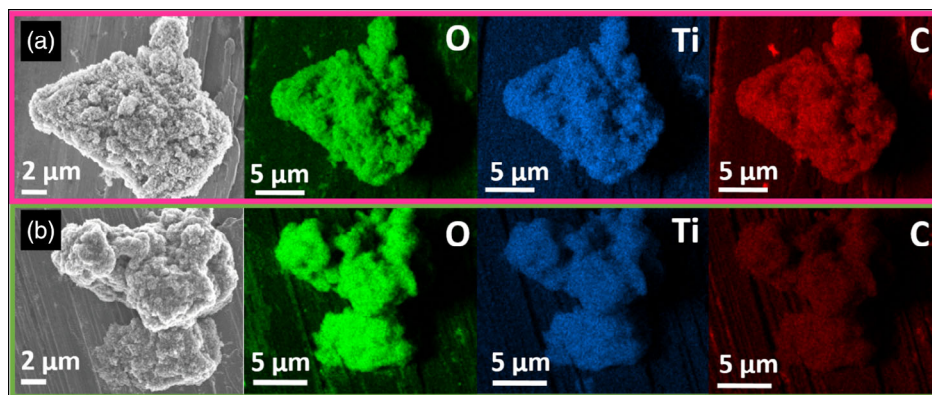


Figure 3. SEM images of a) A50R50 and b) A90R10 and the corresponding EDX mapping analysis for oxygen (in green), titanium (in blue), and carbon (in red).

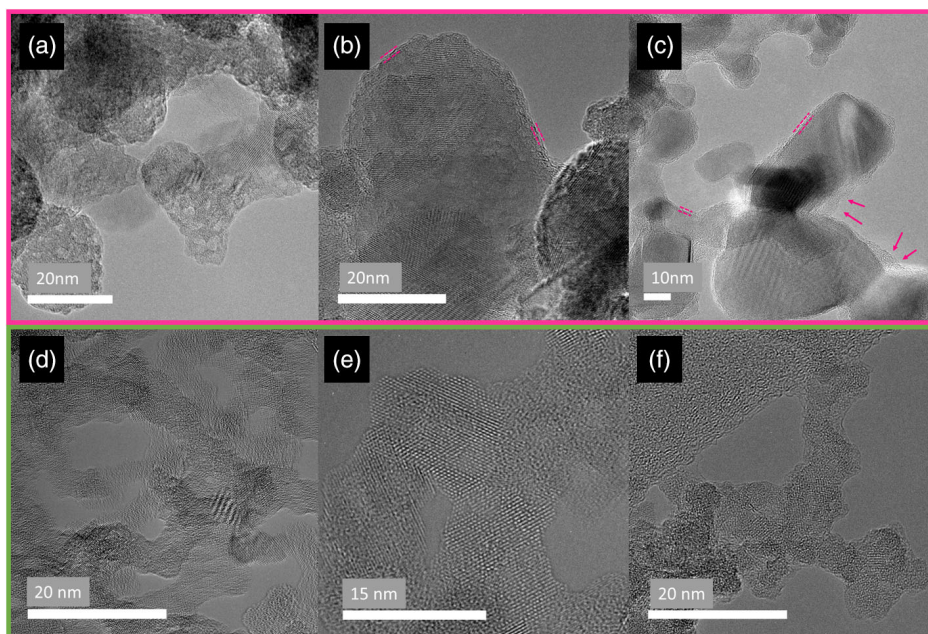


Figure 4. HRTEM images of a–c) A50R50 (pink frame) and d–f) A90R10 (green frame) at varying sample positions and magnifications. Equally colored arrows indicate the detection of thin amorphous layers on the crystallite surface, which may be attributed to the remaining carbon in the two samples.

was observed at the particle surface, which is assigned to the presence of carbon remaining from the synthesis, forming a rather homogeneous coating at the particle surface (Figure 4b,c). In fact, via thermogravimetric analysis (TGA), we determined an overall carbon content of 6.5 wt% in A50R50 (Figure S1, Supporting Information). Generally, the very random crystalline orientation suggests that the anatase and rutile phases are well intermixed within the material. A90R10 appears even more crystallized (Figure 4d,e), whereas the aforementioned nanoscale porosity/amount of defects is much lower. The significantly decreased presence of amorphous phases and the frequent highly crystalline edges of the nanoparticles, accompanied by a few particles with a very thin amorphous surface layer (Figure 4f), are in good agreement with the significantly lower amount of carbon remaining in this material, i.e., about 3.9 wt% as determined by TGA (Figure S1, Supporting Information), and this correlates well with the lower mass flow rate of C_2H_4 in this case.

2.2. Electrochemical Characterization

To understand the impact of the different anatase-to-rutile ratios on the electrochemical behavior, electrodes based on A90R10 and A50R50 were subjected to cyclic voltammetry (CV) measurements in three-electrode half cells. The comparison of the three initial cyclic sweeps for the two materials at a rather low sweep rate of 0.05 mV s^{-1} is shown in Figure 5a. Generally, both materials reveal a very similar shape with the two main redox peaks for cathodic reduction (lithiation) and anodic oxidation (delithiation) of anatase TiO_2 between 1.6 and 1.7 V and between 1.9 and 2.0 V, respectively.^[28] The peak intensity, especially for the anodic peak, is higher for A90R10, which is assigned to the higher ratio of

the anatase phase. More interestingly, the peak separation is narrower for A90R10, which indicates enhanced kinetics for the corresponding redox reaction in A90R10. The contribution of the rutile phase is difficult to be extracted from these CV data, as the redox potential of the main—though commonly rather broad and less intensive—peak couple is located at very similar values.^[22,48] However, there is a rather clear indication of the increased presence of rutile TiO_2 in A50R50: a relatively small (essentially irreversible) anodic peak at around 1.4 V, which was assigned to the irreversible phase transition from (rutile) TiO_2 to Li_1TiO_2 .^[22] In contrast, A90R10 shows a very broad cathodic peak at about 1.5 V and, generally, a higher current flowing at potentials prior to the main anodic peak, which might indicate the second phase transition from titanate to anatase Li_1TiO_2 .^[26–29] In addition, A90R10 reveals rather small cathodic and anodic peaks in the region at around 1.45–1.6 V, which is the characteristic signature of $TiO_2(B)$.^[49–52] The detection of this phase by XRD, however, is difficult, especially if present only in minor traces, due to the great overlap with the main reflections of the anatase phase.^[51,53] When step-wise increasing the sweep rate up to 1.5 mV s^{-1} (Figure 5b,c), all these findings become even more apparent. In the case of A50R50 (Figure 5b), the peak separation gradually increases up to about 0.5 V, whereas the characteristic signature of $TiO_2(B)$ is also observed at high rates. In the case of A90R10 (Figure 5c), the increase in peak separation (0.4 V) is substantially less pronounced, further suggesting enhanced kinetics, the greater overall current, and the apparent “fingerprint” redox features belonging to $TiO_2(B)$. In addition to this rather qualitative analysis, this experiment also allows for the determination of the apparent lithium-ion diffusion coefficient by applying the simplified Randles–Sevcik equation (2) for the main redox couple.^[54,55]

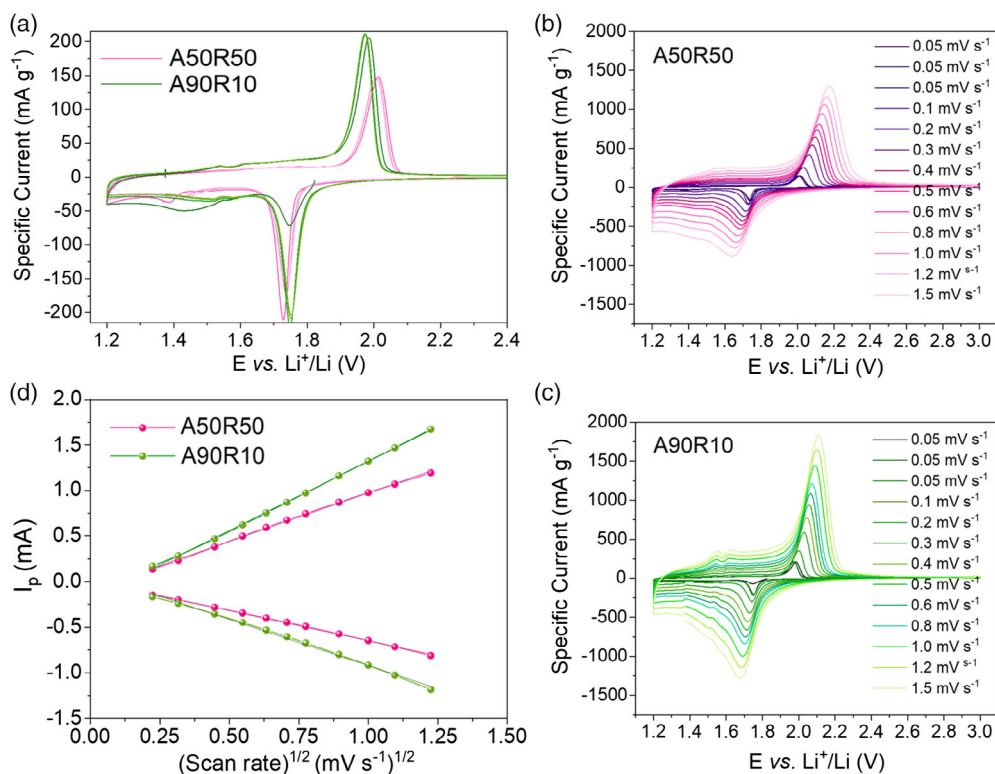


Figure 5. Comparative electrochemical analysis of electrodes based on A50R50 (in pink) and A90R10 (in green) via cyclic voltammetry: a) Plot of the first three cyclic sweeps at 0.05 mV s^{-1} ; b,c) plot of the continuous cyclic sweeps at elevated sweep rates, ranging from 0.05 to 1.5 mV s^{-1} , for electrodes based on (b) A50R50 and (c) A90R10. d) Plot of the linear response of the peak current intensity as a function of the square root of the sweep rate for the two samples (reversing potentials: 1.2 and 3.0 V).

$$I_p = 2.68 \times 10n^{3/2}AD^{1/2}C\omega^{1/2} \quad (2)$$

with I_p is the peak current intensity, n is the number of the involved electrons, A is the electrode area (1.13 cm^2 , which is apparently a simplification given the porous electrode morphology), C is the molar concentration of lithium ions in our sample (we used a constant value of 1 in both cases for a qualitative comparison), ω is the applied scan rate, and D is the apparent lithium-ion diffusion coefficient. The results of this analysis are shown in Figure 5d, providing a plot of the linear response of the peak current intensity as a function of the square root of the sweep rate. Based on data extrapolated from this plot, the apparent lithium-ion diffusion coefficients were calculated to be $7.0 \times 10^{-8} \text{ cm}^2 \text{ s}^{-1}$ and $2.7 \times 10^{-8} \text{ cm}^2 \text{ s}^{-1}$ for the delithiation and lithiation of A50R50. For A90R10, the values obtained are significantly higher with 1.4×10^{-7} and $6.4 \times 10^{-8} \text{ cm}^2 \text{ s}^{-1}$ for delithiation and lithiation, respectively. This difference is generally in line with the limited (essentially 1D) Li^+ diffusion kinetics in bulk rutile TiO_2 ($\approx 10^{-6} \text{ cm}^2 \text{ s}^{-1}$ along the c -axis and about $10^{-15} \text{ cm}^2 \text{ s}^{-1}$ along the a - and b -axis, decreasing with an increasing lithium content^{[56])} compared with the anatase phase ($\approx 10^{-12}$ – $10^{-16} \text{ cm}^2 \text{ s}^{-1}$, no preferential diffusion direction).^[12,14–16,48,57–61] Moreover, the extended presence of phase boundaries in A50R50 might additionally hamper the charge transport along with the aforementioned nanoscale porosity—at least if these pores/defects are not accessible for the electrolyte.

Regarding the absolute values, we may note here that these do not directly represent lithium diffusivity within the single TiO_2 nanoparticle(s) but only serve for a direct comparison between the two samples to highlight the impact of the different anatase-to-rutile ratios, considering that all external parameters (i.e., the cell setup, electrode composition, mass loading, current collector, electrolytes, separator, etc.) have been kept essentially the same in both cases. In fact, the different orders of magnitude indicate that the determined values are largely affected by the aforementioned experimental parameters (a relatively high fraction of conductive carbon and light active material mass loading in combination with a presumably high electrode porosity and, thus, electrolyte infiltration, as the electrodes have not been pressed).

Following this rather analytical electrochemical investigation of the two materials, we conducted in a subsequent step galvanostatic cycling experiments (Figure 6a). The first cycle was conducted at a rather low C rate of 0.05 C . The corresponding dis-/charge profiles (Figure 6b) reflect the CV results. The voltage plateau at about 1.7 V , related to the first phase transition of anatase TiO_2 ,^[25,26,62] is longer for A90R10 due to the larger fraction of the anatase phase. The subsequent slope at lower voltages is gentler for A90R10, which is attributed to the more pronounced occurrence of the second phase transition^[26,28] and the slightly higher presence of $\text{TiO}_2(\text{B})$.^[49,51] Upon delithiation, the same features are observed, highlighting

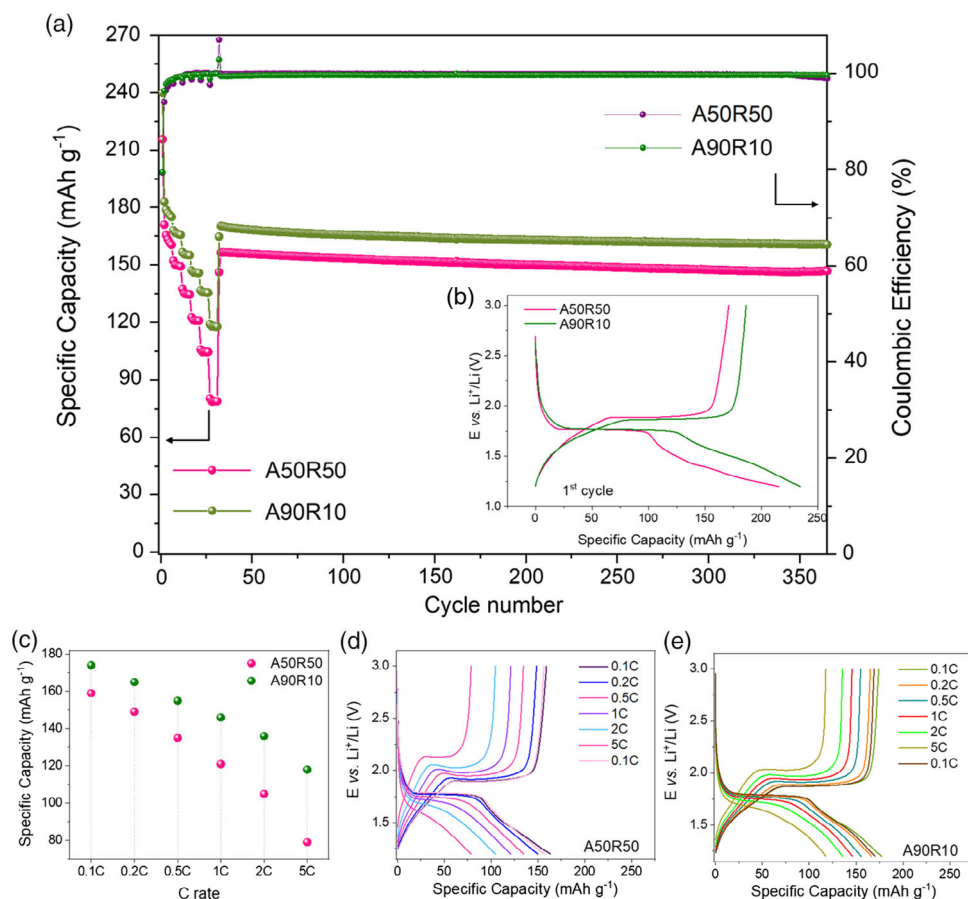


Figure 6. a) Comparison of the rate capability of electrodes based on A50R50 and A90R10 (same color coding as above) at varying dis-/charge rates from 0.05 C (first cycle) over 0.1, 0.2, 0.5, 1, and 2 C up to 5 C (every five cycle) and the subsequent cycling stability at 0.1 C—plotted along with the Coulombic efficiency for both materials; in inset b), the first cycle's dis-/charge profiles for the two samples at 0.05 C are shown. c) Comparative summary of the specific capacity provided by A50R50 and A90R10 at varying C rates. d,e) The plot of representative dis-/charge profiles at varying C rates for (c) A50R50 and (d) A90R10 (cut-off voltages: 1.2 and 3.0 V).

the reversibility of these processes, just like the slightly superior first-cycle Coulombic efficiency of A90R10 (79.5% vs 79.3%). As a result, electrodes based on A90R10 provide a reversible specific capacity of 186 mAh g⁻¹ (Li_{0.55}TiO₂) in the first cycle, which is significantly higher than the specific capacity of 171 mAh g⁻¹ (Li_{0.51}TiO₂) recorded for A50R50. The higher specific capacity is assigned to the reduced presence of the rutile phase, which is generally characterized by a lower lithium uptake.^[16] In fact, considering the reported maximum lithiation capacity ratio of 0.85:1.0 for nanoparticulate rutile:anatase,^[16] one would expect a maximum theoretical capacity of about 310 and 330 mAh g⁻¹ for A50R50 and A90R10, respectively, at least for sufficiently small particles (in the range of a few nanometers), as discussed earlier. For nanoparticles with a diameter of up to about 50 nm, the observed difference and total capacity is well within the anticipated range, whereas the lithium uptake exceeding 0.5 lithium per formula unit TiO₂, specifically in the case of A90R10, is in line with the previous study on carbon-coated TiO₂ nanoparticles, benefitting from the additional phase transition in the near-surface region of the particle.^[26–29,39–42]

After the first cycle, a series of step-wise increasing specific currents was applied to test whether the materials can stand fast dis-/charge rates (Figure 6a,c and Table S1, Supporting Information). The electrodes based on A90R10 show substantially higher specific capacities at all C rates. For instance, at 5 C, A90R10 provides a reversible specific capacity of about 118 mAh g⁻¹ compared to only 79 mAh g⁻¹ for A50R50. This greater rate capability is in line with the higher apparent lithium-ion diffusion coefficient determined for electrodes based on A90R10 and the relatively lower overpotential when applying elevated C rates for A90R10 (compare Figure 6d,e). Interestingly, also the initial nucleation barrier when entering the main voltage plateau upon delithiation is much less pronounced for A90R10, further highlighting the favorable de-/lithiation kinetics. After this evaluation of the rate capability, the dis-/charge rate was decreased back to 0.1 C with very good capacity retention for both samples. However, the cycling stability is better for A90R10, as apparent from the increasing gap between the two capacity plots (Figure 6a), leading to a capacity retention of 95.2% and 94.0% after more than 300 cycles at 0.1 C for A90R10 and A50R50, respectively.

3. Conclusion

Laser pyrolysis is an easily scalable synthesis method for the single-step preparation of carbon-coated TiO₂ nanoparticles. It has been shown that the careful adjustment of the mass flow rate of the C₂H₄ sensitizer plays a decisive role for the eventual crystal structure, i.e., a lower flow rate led to a substantially increased fraction of the anatase phase as a result of the lower reaction temperature. This increased anatase-to-rutile ratio (90:10 vs 50:50) allows for enhanced de-/lithiation kinetics, higher capacities, and improved cycling stability, underlining the critical importance of suppressing the presence of the rutile phase. It is anticipated that this synthesis method is generally applicable also for the single-step synthesis of other carbon-coated and nanosized LIB active materials following the fine tuning of the synthesis parameters.

4. Experimental Section

Synthesis: Two different nanosized titanium dioxide (TiO₂) materials were synthesized by laser pyrolysis, following a similar procedure as described in previous studies.^[46,63,64] In brief, this synthesis was based on the resonance of the emission of a CO₂ laser with the chemical precursors. In the present case, liquid titanium (IV) tetraisopropoxide (TTIP, Sigma-Aldrich, ≥97% purity) was used as the titanium precursor. An aerosol composed of TTIP droplets was generated using a Pyrosol device (RBI, Meylan France). The thus formed droplets were transported via argon, serving as the carrier gas (2000 mL min⁻¹), to a reactor at about 98.7 kPa, where they intersected with the beam of a high-power CO₂ laser (maximum emission at 10.6 μm). During the experiment, the internal power of the laser was tuned at 530 W and the temperature of the TTIP precursor in the Pyrosol was regulated at 20 °C. As TTIP poorly absorbed laser radiation, C₂H₄ was added as the sensitizer to the carrier gas due to its efficient absorption at that specific wavelength, enabling the efficient dissociation of TTIP and the growth of nanoparticles in the reaction zone (defined as the intersection of the laser beam and the flow of TTIP and C₂H₄). The decomposition of the precursors and the growth of the nanoparticles were accompanied by the appearance of a flame in the reaction zone. Potential parameters to tune the properties and characteristics of the final product were, for instance, laser power^[47] and the sensitizer mass flow rate. In this work, we investigated the impact of the latter parameter. The flow of the sensitizer was set at 355 sccm for the first sample labeled A50R50, whereas it was 300 sccm for the second sample labeled A90R10. The experimental conditions were constant all along the duration of the synthesis (90 min). The resulting powders were collected downstream on porous metallic filters and stored in containers in air atmosphere till use.

Physicochemical Characterization: The obtained samples were characterized via powder XRD using a Bruker D8 Advance operating with Cu Kα radiation (λ = 0.154 nm). Diffractograms were recorded in the 2θ range of 15–115° with a step size of 0.02° and a counting time per step of 1.45 s. The diffractograms were analyzed using the GSAS software. TGA (TA Instruments Q5000) was conducted in O₂ atmosphere to determine the amount of carbon in the samples, applying a heating rate of 3 °C min⁻¹ in the range from 30 to 450 °C. The particle morphology and chemical composition were studied by SEM (Zeiss Crossbeam 340 field-emission electron microscope) in combination with EDX (Oxford Instruments X-MaxN EDX spectrometer) and HRTEM (with the image Cs-aberration-corrected TEM FEI Titan 80-300 working at 300 kV or with a JEOL 2010 TEM operated at 200 kV).

Electrode Preparation, Cell Assembly, and Electrochemical Characterization: The materials were used as synthesized. Electrodes were prepared with a composition of 70:20:10 in weight for the active material, conductive carbon (Super C65®, IMERYs), and the binder (sodium

carboxymethyl cellulose, CMC, Dow-Wolff Cellulosics), respectively. The binder was initially dissolved in deionized water.^[65,66] Subsequently, the active material and conductive carbon were added. The resulting mixture was dispersed for 2 h by means of a planetary ball mill (Pulverisette 4, Fritsch). The thus obtained slurry was cast with a wet film of thickness 150 μm on a dendritic copper foil (Schlenk, 99.9%), using a laboratory-scale doctor blade. After drying overnight at room temperature, discs of 12 mm in diameter were cut and dried for 24 h in vacuum at 120 °C. The average active material mass loading was around 1.5 mg cm⁻². The cell assembly was conducted in an argon-filled glove box (MBraun UNILab) with H₂O and O₂ content lower than 0.01 ppm. Two different kinds of cells were used for the electrochemical measurements: three-electrode Swagelok-type cells for conducting CV tests and two-electrode 2032 coin cells (Hohsen) for galvanostatic cycling tests. Lithium foil (Honjo, battery grade) was used as a counter and reference electrodes. GF/D glass fiber sheets served as the separator and 1 M LiPF₆ in a 1:1 mixture of ethylene carbonate (EC) and dimethyl carbonate (DMC) as the electrolyte. CV was conducted using a VMP-3 potentiostat (BioLogic). The initial three cyclic sweeps were conducted with a sweep rate of 0.05 mV s⁻¹, followed by additional cyclic sweeps at elevated sweep rates, ranging from 0.1 to 1.5 mV s⁻¹. Galvanostatic cycling was conducted utilizing a Maccor Battery Tester 4300. A dis-/charge rate of 1 C corresponded to a specific current of 168 mA g⁻¹ (considering the capacity of 0.5 lithium per TiO₂ unit). In both cases, the cells were allowed to rest for 12 h prior to the experiments and the temperature was maintained stable at 20 ± 1 °C. The cut-off voltages were set to 1.2 V and 3.0 V versus Li⁺/Li.

Acknowledgements

A.B., S.P., and D.B. acknowledge financial support from the Vector Foundation within the NEW E² project and the Helmholtz Association. R.B. is grateful for the Ph.D. grant from IDEX Paris-Saclay and from the ANR-10-LABX-0074 SigmaLim LabEX in Limoges.

Open access funding enabled and organized by Projekt DEAL.

Conflict of Interest

The authors declare no conflict of interest.

Data Availability Statement

The data that support the findings of this study are available from the corresponding authors upon reasonable request.

Keywords

anatase, laser pyrolysis, lithium-ion batteries, rutile, TiO₂

Received: December 5, 2020

Revised: January 16, 2021

Published online: February 24, 2021

- [1] B. Scrosati, *J. Solid State Electrochem.* **2011**, *15*, 1623.
- [2] M. Li, J. Lu, Z. Chen, K. Amine, *Adv. Mater.* **2018**, *30*, 1800561.
- [3] B. Nykvist, M. Nilsson, *Nat. Clim. Change* **2015**, *5*, 329.
- [4] M. Armand, P. Axmann, D. Bresser, M. Copley, K. Edström, C. Ekberg, D. Guyomard, B. Lestriez, P. Novák, M. Petranikova, W. Porcher, S. Trabesinger, M. Wohlfahrt-Mehrens, H. Zhang, *J. Power Sources* **2020**, *479*, 228708.
- [5] Z. Chen, I. Belharouak, Y.-K. Sun, K. Amine, *Adv. Funct. Mater.* **2013**, *23*, 959.

- [6] D. Bresser, E. Paillard, M. Copley, P. Bishop, M. Winter, S. Passerini, *J. Power Sources* **2012**, 219, 217.
- [7] M. Madian, A. Eychemüller, L. Giebeler, *Batteries* **2018**, 4, 7.
- [8] D. Bresser, G.-T. Kim, E. Binetti, M. Striccoli, R. Comparelli, S. Seidel, D. Ozkaya, M. Copley, P. Bishop, E. Paillard, S. Passerini, *J. Power Sources* **2015**, 294, 406.
- [9] R. Wagner, N. Preschitschek, S. Passerini, J. Leker, M. Winter, *J. Appl. Electrochem.* **2013**, 43, 481.
- [10] Y. Liu, Y. Yang, *J. Nanomater.* **2016**, 2016, 1.
- [11] Z. Yang, D. Choi, S. Kerisit, K. M. Rosso, D. Wang, J. Zhang, G. Graff, J. Liu, *J. Power Sources* **2009**, 192, 588.
- [12] Y. Zhang, Y. Tang, W. Li, X. Chen, *ChemNanoMat* **2016**, 2, 764.
- [13] T. Ohzuku, A. Ueda, N. Yamamoto, *J. Electrochem. Soc.* **1995**, 142, 1431.
- [14] D. Deng, M. G. Kim, J. Y. Lee, J. Cho, *Energy Environ. Sci.* **2009**, 2, 818.
- [15] X. Yan, Z. Wang, M. He, Z. Hou, T. Xia, G. Liu, X. Chen, *Energy Technol.* **2015**, 3, 801.
- [16] V. Aravindan, Y.-S. Lee, R. Yazami, S. Madhavi, *Mater. Today* **2015**, 18, 345.
- [17] M. B. Vazquez-Santos, P. Tartaj, E. Morales, J. M. Amarilla, *Chem. Rec.* **2018**, 18, 1178.
- [18] X. Han, M. Ouyang, L. Lu, J. Li, *Energies* **2014**, 7, 4895.
- [19] T. Froeschl, U. Hormann, P. Kubiak, G. Kucerova, M. Pfanzelt, C. K. Weiss, R. J. Behm, N. Hüsing, U. Kaiser, K. Landfester, M. Wohlfahrt-Mehrens, *Chem. Soc. Rev.* **2012**, 41, 5313.
- [20] X. Li, F. Zhang, B. Zhai, X. Wang, J. Zhao, Z. Wang, *J. Phys. Chem. Solids* **2020**, 145, 109552.
- [21] Y.-S. Hu, L. Kienle, Y.-G. Guo, J. Maier, *Adv. Mater.* **2006**, 18, 1421.
- [22] P. Kubiak, M. Pfanzelt, J. Geserick, U. Hörmann, N. Hüsing, U. Kaiser, M. Wohlfahrt-Mehrens, *J. Power Sources* **2009**, 194, 1099.
- [23] G. Sudant, E. Baudrin, D. Larcher, J.-M. Tarascon, *J. Mater. Chem.* **2005**, 15, 1263.
- [24] M. Wagemaker, R. van de Krol, A. P. M. Kentgens, A. A. van Well, F. M. Mulder, *J. Am. Chem. Soc.* **2001**, 123, 11454.
- [25] R. J. Cava, D. W. Murphy, S. Zahurak, A. Santoro, R. S. Roth, *J. Solid State Chem.* **1984**, 53, 64.
- [26] M. Wagemaker, W. J. H. Borghols, F. M. Mulder, *J. Am. Chem. Soc.* **2007**, 129, 4323.
- [27] W. J. H. Borghols, D. Lutzenkirchen-Hecht, U. Haake, E. R. H. van Eck, F. M. Mulder, M. Wagemaker, *Phys. Chem. Chem. Phys.* **2009**, 11, 5742.
- [28] D. Bresser, E. Paillard, E. Binetti, S. Krueger, M. Striccoli, M. Winter, S. Passerini, *J. Power Sources* **2012**, 206, 301.
- [29] N. J. J. de Klerk, A. Vasileiadis, R. B. Smith, M. Z. Bazant, M. Wagemaker, *Phys. Rev. Mater.* **2017**, 1, 025404.
- [30] M. R. Ranade, A. Navrotsky, H. Z. Zhang, J. F. Banfield, S. H. Elder, A. Zaban, P. H. Borse, S. K. Kulkarni, G. S. Doran, H. J. Whitfield, *Proc. Natl. Acad. Sci. U. S. A* **2002**, 99, 6476.
- [31] A. A. Levchenko, G. Li, J. Boerio-Goates, B. F. Woodfield, A. Navrotsky, *Chem. Mater.* **2006**, 18, 6324.
- [32] D. J. Reidy, J. D. Holmes, M. A. Morris, *J. Eur. Ceram. Soc.* **2006**, 26, 1527.
- [33] W. Devina, D. Nam, J. Hwang, C. Chandra, W. Chang, J. Kim, *Electrochim. Acta* **2019**, 321, 134639.
- [34] N. Kim, M. R. Raj, G. Lee, *Nanotechnology* **2020**, 31, 415401.
- [35] D. Y. Rhee, J. Kim, J. Moon, M.-S. Park, *J. Alloys Compd.* **2020**, 843, 156042.
- [36] C. Zhang, S. Liu, Y. Qi, F. Cui, X. Yang, *Chem. Eng. J.* **2018**, 351, 825.
- [37] Q. Chen, Y. F. Yuan, S. M. Yin, M. Zhu, G. S. Cai, *Nanotechnology* **2020**, 31, 435410.
- [38] Y. Liu, T. Ding, D. Shen, J. Dou, M. Wei, *J. Electroanal. Chem.* **2017**, 804, 87.
- [39] B. Oschmann, D. Bresser, M. N. Tahir, K. Fischer, W. Tremel, S. Passerini, R. Zentel, *Macromol. Rapid Commun.* **2013**, 34, 1693.
- [40] D. Bresser, B. Oschmann, M. N. Tahir, W. Tremel, R. Zentel, S. Passerini, *J. Power Sources* **2014**, 248, 852.
- [41] S.-J. Park, Y.-J. Kim, H. Lee, *J. Power Sources* **2011**, 196, 5133.
- [42] J. U. Ha, J. Lee, M. A. Abbas, M. D. Lee, J. Lee, J. H. Bang, *ACS Appl. Mater. Interfaces* **2019**, 11, 11391.
- [43] X. Deng, Z. Wei, C. Cui, Q. Liu, C. Wang, J. Ma, *J. Mater. Chem. A* **2018**, 6, 4013.
- [44] <https://www.nanomakers.fr/> (accessed: December 2020).
- [45] M. T. Swihart, *Curr. Opin. Colloid Interface Sci.* **2003**, 8, 127.
- [46] J. Wang, Y. Lin, M. Pinault, A. Filoramo, M. Fabert, B. Ratier, J. Bouclé, N. Herlin-Boime, *ACS Appl. Mater. Interfaces* **2015**, 7, 51.
- [47] B. Pignon, H. Maskrot, V. Guyot Ferreol, Y. Leconte, S. Coste, M. Gervais, T. Pouget, C. Reynaud, J.-F. Tranchant, N. Herlin-Boime, *Eur. J. Inorg. Chem.* **2008**, 2008, 883.
- [48] E. Baudrin, S. Cassaignon, M. Koelsch, J.-P. Jolivet, L. Dupont, J.-M. Tarascon, *Electrochem. Commun.* **2007**, 9, 337.
- [49] M. Zukulová, M. Kalbáč, L. Kavan, I. Exnar, M. Graetzel, *Chem. Mater.* **2005**, 17, 1248.
- [50] A. G. Dylla, G. Henkelman, K. J. Stevenson, *Acc. Chem. Res.* **2013**, 46, 1104.
- [51] B. Laskova, M. Zukulova, A. Zukal, M. Bousa, L. Kavan, *J. Power Sources* **2014**, 246, 103.
- [52] D. P. Opra, S. V. Gnedenkov, S. L. Sinebryukhov, *J. Power Sources* **2019**, 442, 227225.
- [53] A. R. Armstrong, G. Armstrong, J. Canales, P. G. Bruce, *Angew. Chem., Int. Ed.* **2004**, 43, 2286.
- [54] C.-K. Park, S.-B. Park, H.-C. Shin, W. I. Cho, H. Jang, *Bull. Korean Chem. Soc.* **2011**, 32, 191.
- [55] Z. Chen, G.-T. Kim, D. Bresser, T. Diemant, J. Asenbauer, S. Jeong, M. Copley, R. J. Behm, J. Lin, Z. Shen, S. Passerini, *Adv. Mater. (Weinheim, Ger.)* **2018**, 8, 1801573.
- [56] S. Bach, J. P. Pereira-Ramos, P. Willman, *Electrochim. Acta* **2010**, 55, 4952.
- [57] O. W. Johnson, *Phys. Rev.* **1964**, 136, A284.
- [58] Z. Yang, D. Choi, S. Kerisit, K. M. Rosso, D. Wang, J. Zhang, G. Graff, J. Liu, *J. Power Sources* **2009**, 192, 588.
- [59] D. Imazeki, C. C. van Gils, K. Nishio, R. Shimizu, T. Hitosugi, *ACS Appl. Energy Mater.* **2020**, 3, 8338.
- [60] Z. Ma, X. Gao, Z. She, M. A. Pope, Y. Li, *ChemElectroChem* **2020**, 7, 4124.
- [61] M. L. Sushko, K. M. Rosso, J. Liu, *J. Phys. Chem. C* **2010**, 114, 20277.
- [62] S. S. El-Deen, A. M. Hashem, A. E. Abdel Ghany, S. Indris, H. Ehrenberg, A. Mauger, C. M. Julien, *Ionics* **2018**, 24, 2925.
- [63] R. Belchi, A. Habert, E. Foy, A. Gheno, S. Vedraïne, R. Antony, B. Ratier, J. Bouclé, N. Herlin-Boime, *ACS Omega* **2019**, 4, 11906.
- [64] K. Wang, M. Endo-Kimura, R. Belchi, D. Zhang, A. Habert, J. Bouclé, B. Ohtani, E. Kowalska, N. Herlin-Boime, *Materials* **2019**, 12, 4158.
- [65] M. Mancini, F. Nobili, R. Tossici, M. Wohlfahrt-Mehrens, R. Marassi, *J. Power Sources* **2011**, 196, 9665.
- [66] A. Moretti, G.-T. Kim, D. Bresser, K. Renger, E. Paillard, R. Marassi, M. Winter, S. Passerini, *J. Power Sources* **2013**, 221, 419.